proportional to the projection of the eigenvector on $\boldsymbol{q}$. In X-ray scattering in the 0.1-nm wavelength region, this contribution is fairly simple because it is directly obtained from the phonon eigenvectors tightly related to the nuclear crystal symmetry. In the case of the scattering at relatively low energy, and at an energy close to an absorption edge, $\boldsymbol{F_{qj}} \cdot \boldsymbol{q}$ contains much more information because the structure factor vector $\boldsymbol{F_{qj}}$ depends on both the ground and excited electron states. That makes the experiments more demanding but also provides a means for the investigation of complex materials and better validation of the theoretical estimates of the real and imaginary parts of the scattering factors. In the present case one can assume that, among the twelve modes of HOPG at each $\boldsymbol{q}$, the only ones contributing significantly are the longitudinal acoustic mode (LA, $\omega_{\boldsymbol{qj}} \simeq c_l(\hat{\boldsymbol{q}})q$) and the lowest energy longitudinal optic mode (LO, $\omega_{\boldsymbol{qj}} \approx$ const.) (36–38). The LA dispersion is known to be strongly anisotropic as the sound velocity c_l is $c_l^{(c)} = 2.38$ meV nm = 3,620 m/s along the unique axis and $c_l^{(a)} = 17.1$ meV nm = 25,900 m/s on the hexagonal plane, with negligible direction dependence (39). Notice that the dependence of $c_l(\hat{q})$ on $\hat{q}$ is unknown when its direction is intermediate between the hexagonal plane and the hexagonal axis. Also notice that in $\tilde{n}_{\boldsymbol{qj}}(t)$, we neglect the effect of the finite phonon lifetime ($\gg 1$ ps from the measured lineshape of the LA and LO phonon modes (36, 38)) which is much longer than the incident pulse $f(t)$ duration (≈ 70 fs).

As a preliminary test of the model, in Fig. 1*D*, we show a single exponential fitting to the R_{scat} data. The fit is adequate in the whole I_0 range explored (almost a factor of two) for both wavelengths. Besides the expected exponential trend, the most striking feature in Fig. 1*D* is the change of R_{scat} on varying λ_0. A scale factor of 10 is needed to make R_{scat} at $\lambda_0^{(2)}$ of the same order as that at $\lambda_0^{(1)}$. The energy dependence of R_{scat} is related to some relevant physical parameters: namely, the carbon scattering factor $|f_s(\lambda_0)|^2$, the intensity reduction due to absorption, proportional to $1/\mu(\lambda_0)$, and the sampled region in the BZ $V_{scat}(\lambda_0)$, so that $R_{scat} \propto |f_s|^2 V_{scat}/\mu$. In *SI Appendix*, Page S2, we discuss how the possible assessments a priori of the energy dependence of R_{scat} are characterized by a limited accuracy. We here demonstrate that the present investigation can provide solid quantitative information on the above-mentioned physical quantities, otherwise hardly accessible experimentally.

For a quantitative analysis, a fitting function to the R_{scat} data is elaborated. Since non-linear fitting procedures can produce apparently good results when several correlated parameters are present, we made proper approximations to reduce the number of free parameters. We start from the calculation of $S_{ph}(\boldsymbol{q})$ for the LA and LO phonon modes. We add to it the low-q prescription $S_e(q) \propto (\hbar/2m\omega_p)q^2$, m being the electron mass and ω_p the plasma frequency (40), fixed by comparing to the free atom contribution. Since, as discussed above, the intensities are measured in arbitrary units, we rescale these contributions using proper scale factors for I_0 and for I_{scat}/I_0 from the two phonon modes; the electronic contribution is also rescaled accordingly. Since Eq. **3** contains a time-dependent phonon occupation number, we can use $\tilde{n}_{\boldsymbol{qj}}(t) - \tilde{n}_B(\hbar\omega_{\boldsymbol{qj}}) = n^+(t) - n^-(t)$ to describe its mild growth, because from Eqs. **1** and **2**, a closed form can be derived,

$$\tilde{n}_{\boldsymbol{qj}}(t) = \frac{\tilde{n}_B(\hbar\omega_{\boldsymbol{qj}})\, F_g(t)}{1 - n_0 N_{\boldsymbol{qj}} \int_{-\infty}^{t} f(\tau) F_g(\tau) d\tau} \qquad [4]$$

with $F_g(t) = \exp[n_0 N_{\boldsymbol{qj}} C(\boldsymbol{qj}) \int_{-\infty}^{t} f(\tau) r(\tau) d\tau]$, where we defined $r(t) = \rho(t)/[\rho(t) - 1]$. The fit was thus performed using the following expression:

$$R_{scat} = \sum_{j=1}^{2} A_j \frac{q^2}{\hbar\omega_{\boldsymbol{qj}}} [2\tilde{n}_B(\hbar\omega_{\boldsymbol{qj}}) + 1] \cdot \exp\left\{ B_e I_0 A_j \left[\tilde{n}_{\boldsymbol{qj}} + \frac{\rho(t_f)}{\rho(t_f) + 1} \right] \right\} + A_e A_2\, q^2\, |\epsilon \cdot \epsilon_{\boldsymbol{0}}|^2, \qquad [5]$$

where $j = 1$ and $j = 2$ refer to longitudinal acoustic and optical modes, respectively, and A_e is a normalization constant used to evaluate the (small and fixed) electron scattering contribution, as described above. The two functions $\rho(t_f)$ and $\tilde{n}_{\boldsymbol{qj}}(t)$ are properly adapted from Eqs. **2** and **4** making the following substitution, which allows for a numerical determination: $n_0 N_{\boldsymbol{qj}} C(\boldsymbol{qj}) \Rightarrow I_0 B_e A_j$, and performing numerically the various time integrations in Eq. **4** in the range $[-t_f, +t_f]$. For each phonon mode,

$$A_j = \frac{K}{K_0} \cdot C(\boldsymbol{qj})[2\tilde{n}_B(\hbar\omega_{\boldsymbol{qj}}) + 1],$$

where K and K_0 are the two efficiency constants $K = n(t_f)/I_{scat}$ and $K_0 = n_0/I_0$, while the common growing constant $B_e = N_{\boldsymbol{qj}} K_0$ is the same for all phonon modes. We adopted the phonon dispersion measured in refs. 36 and 38 since a much larger set of data would be needed to take the phonon energies as free parameters. An additional parameter was adopted to describe the (unknown) $c_l(\hat{\boldsymbol{q}})$ change with $\boldsymbol{q}$ direction in terms of a smooth function, connecting the experimentally determined c_l values along the high symmetry directions as asymptotic values. This model well fitted each dataset, typically about 600 experimental points, at four λ_0, ϵ_0 configurations using only three free parameters (A_1, A_2, B_e), dependent on the wavelength and polarization, plus just one fixed parameter to describe the c_l anisotropy (see *SI Appendix*, Page S4, for further discussion). The anisotropy parameter, useful to describe this large body of data and depending on the sample characteristics only, strongly supports the present superradiant model of the coherent radiation scattering: indeed, a possible change in the sample state, produced by the incoming radiation, could not be described using a single parameter. No q dependence was assumed for the phonon structure factor, a choice suggested by the small q range, which is confined well within about 1/3 of the BZ width. Further details on the angular dependence of the scattering data are available in *SI Appendix*, Page S5.

Scattering Amplitudes, Phonon Dispersion, and Coherent Phonon Population. The experimental R_{scat} as a function of θ and I_0 is shown in Fig. 2, where the good agreement with the model is evident. Several quantitative information can be extracted by data fitting and will be described in the following, along with considerations, based on available data on HOPG, that strongly support our analysis and interpretation.

The first very important result is the ratio of the growth coefficients $B_e \propto N_{\boldsymbol{qj}} \propto 1/\mu$ at 4.74 nm to that at 4.08 nm, $b_e = B_e(\lambda_0^{(2)})/B_e(\lambda_0^{(1)})$. It is found $b_{e,p} = 13.64 \pm 0.60$ and $b_{e,s} = 15.17 \pm 0.76$ with vertical and horizontal incoming polarization, respectively. These experimental results are close to the available estimate of the ratio of the linear absorption coefficients equal to 16.7 from the free atom theory (41) and

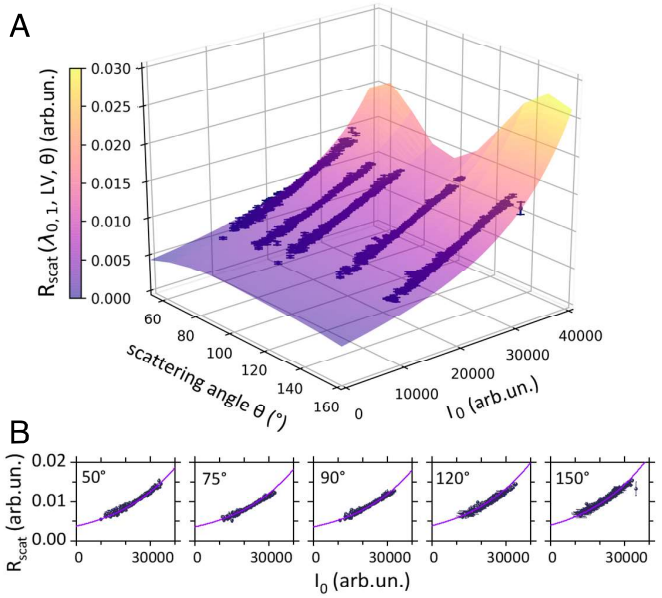

Fig. 2. (*A*) R_{scat} vs. I_0 at different θ (thus, $\boldsymbol{q}$) for $\lambda_0^{(1)} = 4.08$ nm, $\epsilon_0 =$ s. Blue dots: experimental data; surface: data fitting. (*B*) Plots of data and fitting function shown in panel (*A*) for the specific, sampled scattering angles. Similar results are obtained for all the other (λ_0, ϵ_0) datasets.

8.1 from the experimental trends extrapolated from ref. 34; for further details, see *SI Appendix*, Fig. S1 and related comments. That result corroborates the model and introduces an approach for a quantitative determination of μ in bulk materials in this EUV or soft X-ray range.

The second quantitative result is the ratio of the amplitude coefficients A at the two wavelengths, which contains $C(\boldsymbol{qj})$ and thus information on the phonon structure factor (42), for the acoustic and optical modes. The ratios, calculated for both phonons at s and p polarization, give us values close to each other and of the order of 10 (Table 1), providing quantitative indication of the strong wavelength dependence of the scattering factor and polarization factor. On the other side, we find that the ratios of the A coefficients at s and p polarization, calculated for both phonons at $\lambda_0^{(1)}$ and $\lambda_0^{(2)}$, are significantly closer to unit (Table 2), indicating a rather small polarization effect on the amplitudes of the two modes. We recall that at photon energy close to the absorption edge also the polarization dependence of the scattering factors shows an energy dependence (43). It is relevant to notice that the present study can open the door to the determination of both real and imaginary parts of $f_s(\lambda_0)$ in complex materials like graphite. Considering the difficulty of the absolute determination of the linear absorption coefficient by transmission experiments, and of the scattering factors by both experiments and theory, the observed effect opens ways to the study of not only coherent radiation processes

Table 1. Ratios of the amplitude coefficients *A* at $\lambda_0^{(1)}$ and $\lambda_0^{(2)}$ calculated for optic and acoustic phonons (1,2) at s and p polarization

$A_{1,p}(\lambda_0^{(1)})/A_{1,s}(\lambda_0^{(2)})$	11.10 ± 0.26
$A_{2,p}(\lambda_0^{(1)})/A_{2,p}(\lambda_0^{(2)})$	11.82 ± 0.27
$A_{1,s}(\lambda_0^{(1)})/A_{1,s}(\lambda_0^{(2)})$	11.77 ± 0.29
$A_{2,s}(\lambda_0^{(1)})/A_{2,s}(\lambda_0^{(2)})$	8.60 ± 0.24

Table 2. Ratios of the amplitude coefficients *A* at the two polarization s and p calculated for optic and acoustic phonons (1,2) at $\lambda_0^{(1)}$ and $\lambda_0^{(2)}$

$A_{1,p}(\lambda_0^{(1)})/A_{1,s}(\lambda_0^{(1)})$	0.7917 ± 0.0076
$A_{2,p}(\lambda_0^{(1)})/A_{2,s}(\lambda_0^{(1)})$	0.7606 ± 0.0090
$A_{1,p}(\lambda_0^{(2)})/A_{1,s}(\lambda_0^{(2)})$	0.840 ± 0.027
$A_{2,p}(\lambda_0^{(2)})/A_{2,s}(\lambda_0^{(2)})$	0.553 ± 0.019

but also fundamental, and hardly accessible, material properties. Notably, when coherence effects are observed, the information on f_s is contained within both the multiplying coefficient and the exponent of the trend in Eq. **3**, thus providing a more solid experimental estimate of the scattering factor, also considering that the growth coefficient B_e is common to all the phonon modes involved.

It is remarkable that, while the scattered intensity is much lower below the absorption edge, the exponential growth as a function of the incoming intensity, and hence the effect of the coherence, remain similar. Indeed, the exponent factors, proportional to the product of A and B_e, are negligibly reduced ($< 20\%$) at $\lambda_0^{(2)}$ in all the conditions explored. That is in agreement with the description of Eq. **3** and with what is readily observed from the trends in Fig. 1*D*.

From the extrapolation of R_{scat} at $I_0 \to 0$, we infer that the amplitude of $S_{ph}(\boldsymbol{q})$ has a small angular dependence. That occurs because the strong anisotropy of $c_l(\hat{\boldsymbol{q}})$ (see the LA phonon dispersion in Fig. 3, discussed below) produces a decrease of the scattering contribution from the LA mode ($\approx 1/12$) at growing θ, which is compensated by the q^2 increase of the LO part ($\approx \times 5$), an effect independent of polarization and wavelength. Some tests to check for the presence of a structure factor variation suggest that this contribution is smaller than the sensitivity of the experiment, $\approx 10\%$.

The observed variation of $c_l(\hat{\boldsymbol{q}})$ is not in agreement with the trend derived from the graphite elastic constants; therefore, the system is not equivalent to an elastic solid, even if the crystal

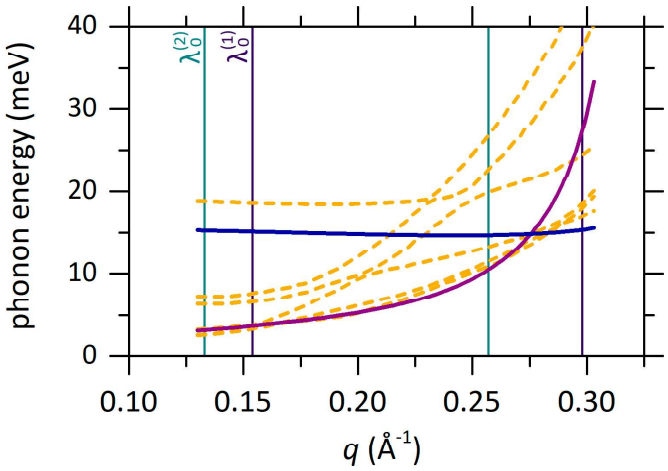

Fig. 3. Phonon dispersion curves (orange dashed lines) calculated by DFT in the transferred q region of interest. The vertical lines mark the q range explored in the experiment with $\lambda_0^{(1)}$ (blue) and $\lambda_0^{(2)}$ (cyan) excitation. The phonon dispersion is calculated performing an average over the possible crystal orientation in HOPG (obtained by rotations about the *c*-axis). The solid lines show the dispersion curves extracted by the fitting of experimental data for the low-energy acoustic (purple) and optical (blue) phonon modes.

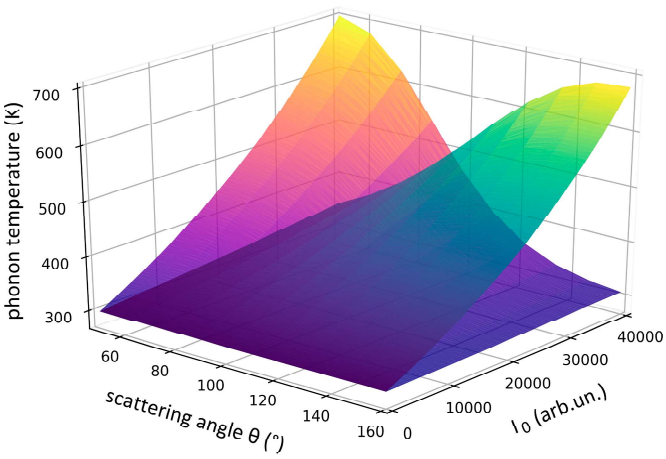

Fig. 4. Phonon temperature versus I_0 and θ calculated from the scattering-modified phonon occupation number for the LO (blue-to-yellow curve, increasing at growing θ) and LA (purple-to-yellow curve) phonon modes. $\tilde{n}_{\boldsymbol{qj}}(t_f)$ is estimated by R_{scat} data fitting for $\lambda_0^{(1)} = 4.08$ nm, ϵ_0 =s.

symmetry is taken into account (39). To have an additional evaluation of the strong anisotropy of $c_l(\hat{\boldsymbol{q}})$ a density functional theory (DFT) calculation was performed using the exchange-correlation potential for the gradient approximation of ref. 44 and the all-electron LAPW (linearized augmented plane wave) DFT code Elk (45). The calculation has been carried out by performing an average of the dispersion relations obtained by rotation around the c-axis. That is necessary because of the random orientations of the small crystallites on the hexagonal plane of HOPG. In principle, only the longitudinal component of the phonon modes can contribute to the scattering in the first BZ. Considering the structure of graphite and the fact that, when the transferred momentum is not along a high symmetry direction, the phonon polarization is neither purely longitudinal nor purely transverse, all the modes tend to contribute here. In Fig. 3, the complex calculated dispersion curves are shown. A qualitative agreement is observed with the model of the fit which uses two major modes only. That result further corroborates both the presented description of the scattering data and its potential applicability in performing new kinds of investigations using more extended sets of experimental configurations. The results show that the experiment can detect the anisotropic bonding of graphene layers in HOPG, while a more extended sampling of the scattering volume is needed to thoroughly assess the aforementioned smaller contributions.

The last remark is on the final phonon state, having the characteristic of a coherent state with a specific change in the average occupation number. According to the model, quantitative information on the increase of $\tilde{n}_{\boldsymbol{qj}}(t)$ by scattering can be extracted from fitting as a by-product. In Fig. 4, we show the increase of the equivalent phonon temperature $T_{\boldsymbol{qj}}$, as estimated from $\tilde{n}_{\boldsymbol{qj}}(t_f)$. An increase of $T_{\boldsymbol{qj}}$ of the order of some hundreds K is estimated for both modes involved. The $T_{\boldsymbol{qj}}$ trends result almost independent of λ_0 , ϵ_0. It is important to observe that the equivalent temperature is just a way to quantify the growth of the phonon occupation number as it is not the thermodynamic temperature. Of course, at later times, once the anharmonic phonon–phonon interaction kicks in, the energy selectively deposited in such low-q hot phonon populations is redistributed among all the vibrational (as well as electronic) degrees of freedom of the system, resulting in a much lower final equilibrium temperature. The different temperatures estimated for the LA and LO phonon populations reflect the selection rules for the modes at varying scattering geometry.

Conclusions

In conclusion, we carried out a Thomson scattering experiment on HOPG exploiting the coherent, ultrashort EUV pulses of FERMI FEL. Here, we find out the evident, crucial role of quantum coherence, as the exponential growth of the scattered intensity upon increasing incident intensity is due to the non-zero commutator of the annihilation and creation operators of the radiation final coherent state. The nonlinearity here paralleling Dicke's theory of superradiance (24, 25) represents a direct laboratory observation of coherence of the scattered EUV radiation, also promoting low-energy coherent phonons in the material, as seen in the exponential trend of $d\sigma/d\Omega|_{ph}$. The QM description of the process provides a precise picture of the data, indicating the way to obtain useful information on the specimen using a wide sampling of the available BZ volume. The present data already provide quantitative results regarding the determination of the absorption in bulk materials and the combined analysis of absorption and scattering factors in the energy region across the absorption edge, other than the study of the anisotropy of sound propagation in graphite.

Our results show that the described framework sets the basis for conceiving EUV Thomson scattering experiments, opening promising routes for material investigations. These experiments could provide information on the properties of condensed matter systems: first, they can give access to basic data, like absorption coefficient in the EUV, scattering factors in crossing the low energy absorption edges, and low-q phonon dispersion curves in thin films. Second, they allow exploring exotic effects, like those produced by superradiant processes triggered by the bright and coherent EUV FEL pulses, combined with the reduced scattering volume in reciprocal space.

Data, Materials, and Software Availability. [txt] data have been deposited in Zenodo (46).

Author affiliations: [a]Dipartimento di Fisica e Geologia, Università di Perugia, Perugia I-06123, Italy; [b]Istituto dei Sistemi Complessi, Consiglio Nazionale delle Ricerche (CNR-ISC), Roma I-00185, Italy; [c]Elettra-Sincrotrone Trieste Società Consortile per Azioni (SCpA), Basovizza, Trieste I-34149, Italy; [d]Dipartimento di Fisica, Sapienza Università di Roma, Roma I-00185 Italy; [e]Istituto Officina dei Materiali, Consiglio Nazionale delle Ricerche (CNR-IOM), Perugia I-06123, Italy; and [f]Area Science Park, Trieste I-34149, Italy

1. W. Heitler, *The quantum theory of radiation* (Courier Corporation, 1984).
2. S. K. Sinha, Theory of inelastic X-ray scattering from condensed matter. *J. Phys.: Condens. Matter* **13**, 7511 (2001).
3. C. Kennel, F. Coroniti, Confinement of the Crab pulsar's wind by its supernova remnant. *Astrophys. J.* **283**, 694–709 (1984).
4. D. Wilson, M. Rees, Induced Compton scattering in pulsar winds. *Mon. Notic. R. Astron. Soc.* **185**, 297–304 (1978).
5. V. Moncrief, Coherent states and quantum nonperturbing measurements. *Ann. Phys.* **114**, 201–214 (1978).
6. P. Emma *et al.*, First lasing and operation of an Ångstrom-wavelength free-electron laser. *Nat. Photon.* **4**, 641–647 (2010).
7. J. Rossbach, J. R. Schneider, W. Wurth, 10 years of pioneering X-ray science at the free-electron laser flash at desy. *Phys. Rep.* **808**, 1–74 (2019).
8. L. Fletcher *et al.*, Ultrabright X-ray laser scattering for dynamic warm dense matter physics. *Nat. Photon.* **9**, 274–279 (2015).
9. T. Ma *et al.*, X-ray scattering measurements of strong ion-ion correlations in shock-compressed aluminum. *Phys. Rev. Lett.* **110**, 065001 (2013).
10. H. Lee *et al.*, X-ray Thomson-scattering measurements of density and temperature in shock-compressed beryllium. *Phys. Rev. Lett.* **102**, 115001 (2009).
11. C. Fortmann *et al.*, Measurement of the adiabatic index in be compressed by counterpropagating shocks. *Phys. Rev. Lett.* **108**, 175006 (2012).

12. J. Valenzuela *et al.*, Measurement of temperature and density using non-collective X-ray Thomson scattering in pulsed power produced warm dense plasmas. *Sci. Rep.* **8**, 1–8 (2018).
13. M. Bonitz, Z. A. Moldabekov, T. Ramazanov, Quantum hydrodynamics for plasmas-Quo vadis? *Phys. Plasmas* **26**, 090601 (2019).
14. S. H. Glenzer, R. Redmer, X-ray thomson scattering in high energy density plasmas. *Rev. Mod. Phys.* **81**, 1625 (2009).
15. A. Höll *et al.*, Thomson scattering from near-solid density plasmas using soft X-ray free electron lasers. *High Energy Density Phys.* **3**, 120–130 (2007).
16. C. Masciovecchio *et al.*, EIS: The scattering beamline at fermi. *J. Synchrot. Radiat.* **22**, 553–564 (2015).
17. M. Trigo *et al.*, Fourier-transform inelastic X-ray scattering from time-and momentum-dependent phonon-phonon correlations. *Nat. Phys.* **9**, 790–794 (2013).
18. M. Kozina *et al.*, Heterodyne X-ray diffuse scattering from coherent phonons. *Struct. Dyn.* **4**, 054305 (2017).
19. C. Fasolato *et al.*, Ultrafast plasmon dynamics in crystalline lif triggered by intense extreme UV pulses. *Phys. Rev. Lett.* **124**, 184801 (2020).
20. M. B. Danailov *et al.*, Towards jitter-free pump-probe measurements at seeded free electron laser facilities. *Opt. Expr.* **22**, 12869–12879 (2014).
21. L. Young *et al.*, Femtosecond electronic response of atoms to ultra-intense X-rays. *Nature* **466**, 56–61 (2010).
22. H. Yoneda *et al.*, Saturable absorption of intense hard X-rays in iron. *Nat. Commun.* **5**, 1–5 (2014).
23. A. Di Cicco *et al.*, Interplay of electron heating and saturable absorption in ultrafast extreme ultraviolet transmission of condensed matter. *Phys. Rev. B* **90**, 220303 (2014).
24. M. Gross, S. Haroche, Superradiance: An essay on the theory of collective spontaneous emission. *Phys. Rep.* **93**, 301–396 (1982).
25. R. H. Dicke, Coherence in spontaneous radiation processes. *Phys. Rev.* **93**, 99 (1954).
26. M. Gross, C. Fabre, P. Pillet, S. Haroche, Observation of near-infrared Dicke superradiance on cascading transitions in atomic sodium. *Phys. Rev. Lett.* **36**, 1035 (1976).
27. T. Torres *et al.*, Rotational superradiant scattering in a vortex flow. *Nat. Phys.* **13**, 833–836 (2017).
28. S. Inouye *et al.*, Superradiant Rayleigh scattering from a Bose-Einstein condensate. *Science* **285**, 571–574 (1999).
29. D. Schneble *et al.*, The onset of matter-wave amplification in a superradiant Bose-Einstein condensate. *Science* **300**, 475–478 (2003).
30. N. Bonini, M. Lazzeri, N. Marzari, F. Mauri, Phonon anharmonicities in graphite and graphene. *Phys. Rev. Lett.* **99**, 176802 (2007).
31. R. J. Glauber, Coherent and incoherent states of the radiation field. *Phys. Rev.* **131**, 2766 (1963).
32. S. Manzeli, D. Ovchinnikov, D. Pasquier, O. V. Yazyev, A. Kis, 2D transition metal dichalcogenides. *Nat. Rev. Mater.* **2**, 1–15 (2017).
33. E. Allaria *et al.*, Highly coherent and stable pulses from the FERMI seeded free-electron laser in the extreme ultraviolet. *Nat. Photon.* **6**, 699–704 (2012).
34. J. A. Brandes *et al.*, Carbon K-edge XANES spectromicroscopy of natural graphite. *Carbon* **46**, 1424–1434 (2008).
35. N. S. Mirian *et al.*, Generation and measurement of intense few-femtosecond superradiant extreme-ultraviolet free-electron laser pulses. *Nat. Photon.* **15**, 523–529 (2021).
36. R. Nicklow, N. Wakabayashi, H. Smith, Lattice dynamics of pyrolytic graphite. *Phys. Rev. B* **5**, 4951 (1972).
37. J. Maultzsch, S. Reich, C. Thomsen, H. Requardt, P. Ordejón, Phonon dispersion in graphite. *Phys. Rev. Lett.* **92**, 075501 (2004).
38. M. Mohr *et al.*, Phonon dispersion of graphite by inelastic X-ray scattering. *Phys. Rev. B* **76**, 035439 (2007).
39. G. Savini *et al.*, Bending modes, elastic constants and mechanical stability of graphitic systems. *Carbon* **49**, 62–69 (2011).
40. D. Pines, P. Nozieres, *The theory of quantum liquids. W. A. Benjamin, inc* (New York, 1966).
41. C. T. Chantler, Theoretical form factor, attenuation, and scattering tabulation for $Z = 1$–92 from $E = 1$–10 eV to $E = 0.4$-1.0 MeV. *J. Phys. Chem. Ref. Data* **24**, 71–643 (1995).
42. B. Willis, Thermal diffuse scattering of X-rays and neutrons. *Int. Tables Crystallogr. B* **4** (1), 484–491 (2010).
43. J. C. Parker, R. Pratt, Validity of common assumptions for anomalous scattering. *Phys. Rev. A* **29**, 152 (1984).
44. J. P. Perdew *et al.*, Restoring the density-gradient expansion for exchange in solids and surfaces. *Phys. Rev. Lett.* **100**, 136406 (2008).
45. Elk code (http://elk.sourceforge.net/) The exchange and correlation potential from ref. (44) was used. The intrinsic disorder of the HOPG planes about the c-axis was accounted for by calculating the dispersion relations along the Γ_M and Γ_K directions. Both are considered to obtain the dispersion curves in Figure 3 (2021).
46. C. Fasolato *et al.*, Experimental data for "Superradiant Thomson scattering from graphite in the extreme ultraviolet". Zenodo. https://doi.org/10.5281/zenodo.7446390. Deposited 29 December 2023.